Monthly Notices of the ROYAL ASTRONOMICAL SOCIETY

MNRAS **501,** 4998–5011 (2021) doi:10.1093/mnras/staa3991
Advance Access publication 2020 December 26

Middle aged γ-ray pulsar J1957+5033 in X-rays: pulsations, thermal emission, and nebula

D. A. Zyuzin [1]★ A. V. Karpova [1] Y. A. Shibanov,[1] A. Y. Potekhin [1] and V. F. Suleimanov[2,3,4]

[1]*Ioffe Institute, Politekhnicheskaya 26, St. Petersburg 194021, Russia*
[2]*Institut für Astronomie und Astrophysik, Sand 1, D-72076 Tübingen, Germany*
[3]*Kazan (Volga region) Federal University, Kremlevskaja str., 18, Kazan 420008, Russia*
[4]*Space Research Institute of the Russian Academy of Sciences, Profsoyuznaya Str. 84/32, Moscow 117997, Russia*

Accepted 2020 December 22. Received 2020 December 22; in original form 2020 October 9

ABSTRACT

We analyse new *XMM–Newton* and archival *Chandra* observations of the middle-aged γ-ray radio-quiet pulsar J1957+5033. We detect, for the first time, X-ray pulsations with the pulsar spin period of the point-like source coinciding by position with the pulsar. This confirms the pulsar nature of the source. In the 0.15–0.5 keV band, there is a single pulse per period and the pulsed fraction is $\approx 18 \pm 6$ per cent. In this band, the pulsar spectrum is dominated by a thermal emission component that likely comes from the entire surface of the neutron star, while at higher energies ($\gtrsim$0.7 keV) it is described by a power law with the photon index $\Gamma \approx 1.6$. We construct new hydrogen atmosphere models for neutron stars with dipole magnetic fields and non-uniform surface temperature distributions with relatively low effective temperatures. We use them in the spectral analysis and derive the pulsar average effective temperature of $\approx(2\text{–}3) \times 10^5$ K. This makes J1957+5033 the coldest among all known thermally emitting neutron stars with ages below 1 Myr. Using the interstellar extinction–distance relation, we constrain the distance to the pulsar in the range of 0.1–1 kpc. We compare the obtained X-ray thermal luminosity with those for other neutron stars and various neutron star cooling models and set some constraints on the latter. We observe a faint trail-like feature, elongated ∼8 arcmin from J1957+5033. Its spectrum can be described by a power law with a photon index $\Gamma = 1.9 \pm 0.5$ suggesting that it is likely a pulsar wind nebula powered by J1957+5033.

Key words: stars: neutron – pulsars: general – pulsars: individual: PSR J1957+5033.

1 INTRODUCTION

Neutron stars (NSs) are born in supernova explosions at very high temperatures $\sim 10^{11}$ K (e.g. Müller 2020, and references therein). They lose the initial thermal energy via neutrino emission from their interiors and then via photon emission from their surfaces (e.g. Yakovlev & Pethick 2004, and references therein). The cooling rate is sensitive to the physical properties of the superdense matter inside NSs, which are still poorly known (e.g. Yakovlev et al. 2005). The equation of state (EoS) of such matter can be constrained by comparison of cooling theories with NSs surface temperatures derived from observational data.

The middle-aged PSR J1957+5033 (hereafter J1957) is a radio-quiet γ-ray pulsar discovered with the *Fermi* Large Area Telescope (LAT) (Saz Parkinson et al. 2010). Its spin period $P = 375$ ms and period derivative $\dot{P} = 7.1 \times 10^{-15}$ s s^{-1} imply the characteristic age $t_c \equiv P/2\dot{P} \approx 840$ kyr, the spin-down luminosity $\dot{E} = 5.3 \times 10^{33}$ erg s^{-1} and the characteristic (spin-down) magnetic field $B = 1.65 \times 10^{12}$ G.[1] The distance to the pulsar is poorly known. The only available estimate, 0.8 kpc, is the so-called 'pseudo-distance' obtained using empirical correlation between the distance and the γ-ray flux above 100 MeV (Abdo et al. 2013). It is known to be uncertain by a factor of 2–3. Analysing the γ-ray pulse profile, Pierbattista et al. (2015) estimated the magnetic inclination and line-of-sight angles of J1957 for different γ-ray emission geometries.

The pulsar X-ray counterpart was identified by position in the 25-ks *Chandra* Advanced CCD Imaging Spectrometer (ACIS-S) observation[2] (Marelli et al. 2015). Its spectrum in the 0.3–10 keV band was found to be well described by the absorbed single power law (PL) with a photon index $\Gamma = 2.1 \pm 0.3$, an energy integrated unabsorbed flux $F_X = (3.0 \pm 0.5) \times 10^{-14}$ erg s^{-1} cm^{-2} and an absorption column density $N_{\rm H} < 2.5 \times 10^{20}$ cm^{-2} (Marelli et al. 2015).

We reanalysed the *Chandra* data and confirmed the results by Marelli et al. (2015). However, we found an unexpectedly large count number in the 0.1–0.3 keV band – 30 against 90 counts detected in the 0.3–10 keV band. This indicates the presence of a second soft component in the pulsar spectrum likely related to the thermal emission from the surface of the NS with a very low effective temperature. In this case, J1957 becomes especially interesting for comparison with NS cooling theories according to which at its characteristic age the pulsar should have already passed from a relatively slow neutrino cooling stage to a significantly faster photon stage where observational

★ E-mail: da.zyuzin@gmail.com

[1]Parameters are calculated using the timing solution for J1957 based on five years of the *Fermi* data obtained from https://confluence.slac.stanford.edu/display/GLAMCOG/LAT+Gamma-ray+Pulsar+Timing+Models. See also Kerr et al. (2015) for details.

[2]ObsID 14828, PI M. Marelli, observation date 2014-02-01.

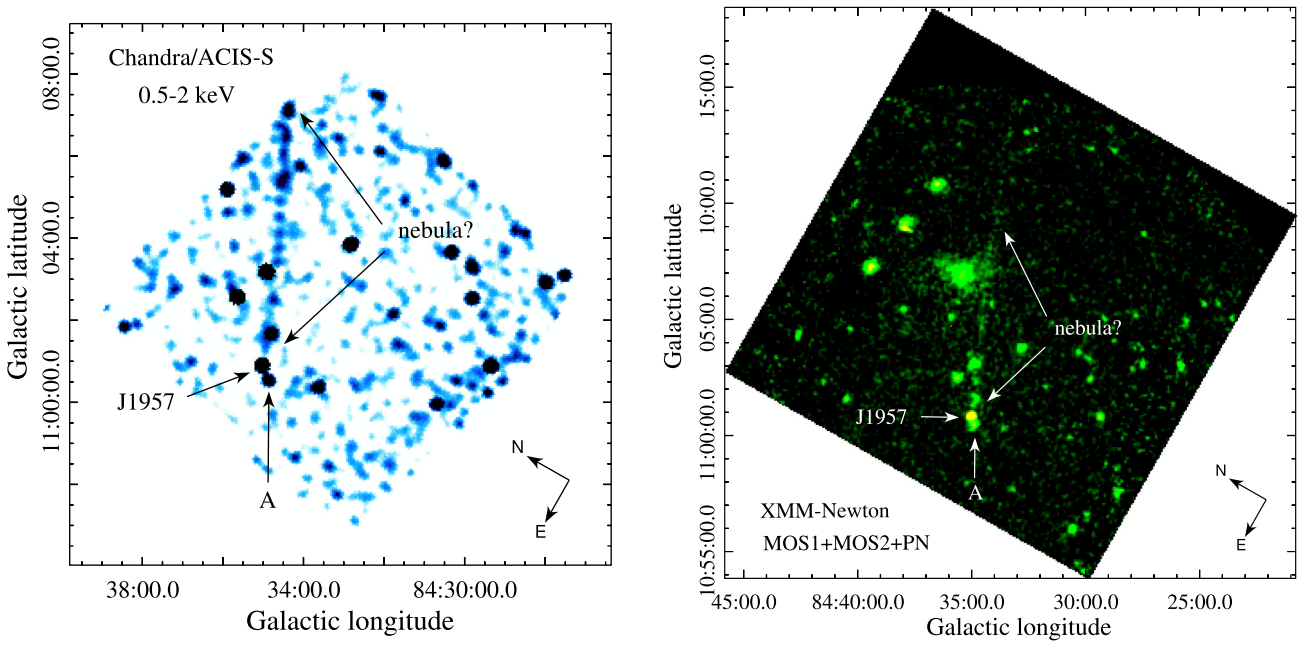

Figure 1. Images of the J1957 field. Left-hand panel: *Chandra* ACIS-S3 chip field-of-view in the 0.5–2 keV band. Right-hand panel: 18 arcmin × 18 arcmin *XMM–Newton* combined MOS1+MOS2+PN image (red = 0.2–0.5 keV, green = 0.5–2 keV). J1957, the nearby star 'A' and the presumed trail-like nebula are marked. Compasses correspond to the equatorial coordinate system.

data on thermal emission from cooling NSs are particularly scarce. Unfortunately, the soft component cannot be confirmed using the *Chandra* data since the ACIS energy scale is not calibrated below 0.3 keV. 3.2 s time resolution of the observations does not also allow to detect pulsations with the pulsar period. Therefore, we performed dedicated *XMM–Newton* observations of J1957. Here we present the analysis of these data. The X-ray data are described in Section 2. Timing and spectral analysis of J1957 are presented in Sections 3 and 4. The results are discussed in Section 5 and summarized in Section 6. Some details of the analysis are given in the Appendices.

2 X-RAY DATA AND IMAGING

The J1957 field was observed with *XMM–Newton* on 2019 October 5 (ObsID 0844930101, PI D. Zyuzin). The total exposure was about 87 ks. The European Photon Imaging Camera Metal Oxide Semiconductor (EPIC-MOS) detectors were operated in the full-frame mode with the imaging area of about 28 arcmin × 28 arcmin and the medium filter and the EPIC-pn camera – in the large window mode with the imaging area of about 13.5 arcmin × 26 arcmin and the thin filter. We also used the *Chandra*/ACIS-S archival data set (ObsID 14828) where the pulsar was exposed on the S3 chip. To analyse the data, we utilized the *XMM–Newton* Science Analysis Software (XMM-SAS) v. 17.0.0 and *Chandra* Interactive Analysis of Observations (CIAO) v. 4.12 packages.

The *Chandra* data set was reprocessed using the CHANDRA_REPRO tool. Applying the FLUXIMAGE task, we created the exposure-corrected image of the ACIS-S3 chip which is presented in the left-hand panel of Fig. 1 where the pulsar counterpart and the nearby star 'A' are marked. The WAVDETECT command was used to obtain coordinates of point-like sources. For J1957, we derived R.A. = $19^{\rm h}57^{\rm m}38\overset{\rm s}{.}390(6)$ and Dec. = $+50^\circ33'21\overset{''}{.}02(5)$ (numbers in parentheses are 1σ pure statistical uncertainties).

We combined the data from both MOS and PN detectors to obtain deeper X-ray images using the 'images' script[3] (Willatt & Ehle 2016). The resulting image is shown in the right-hand panel of Fig. 1. Since *XMM–Newton* has lower spatial resolution than *Chandra*, J1957 is somewhat blurred with the star 'A'. One can see a faint thin feature protruding from J1957 almost perpendicularly to the Galactic plane. It has a clumpy structure and is also visible in the *Chandra* image where it extends up to the edge of the ACIS-S detector (≈6 arcmin). In the *XMM–Newton* image its length seems to be longer, at least up to ∼8 arcmin, though its faintness and some blurring with other sources preclude accurate measurements. This maybe a trail-like pulsar wind nebula (PWN) powered by J1957. One can see that the pulsar is indeed a rather soft source while the presumed PWN is produced by harder photons.

For the further analysis, we filtered out the background flares inspecting high-energy light curves extracted from the field of views (FoVs) of all EPIC detectors. We chose the following threshold count rates to define good time intervals: 0.5 counts s^{-1} for pn and 0.6 counts s^{-1} for both MOS cameras (see Fig. 2). The resulting effective exposures are about 79.8, 79.8, and 48.7 ks for the MOS1, MOS2, and pn detectors, respectively. We selected single to quadruple pixel events (PATTERN ≤12) for the MOS data and single and double pixel events (PATTERN ≤4) for the pn data.

3 TIMING

The timing resolution of the EPIC-pn detector operating in the large window mode is ≈48 ms which allows us to search for pulsations from J1957. We used the event list unfiltered from background flares since multiple time gaps in the data may hamper signal detection. The barycenter correction was applied by the XMM–SAS BARYCEN

[3]https://www.cosmos.esa.int/web/xmm-newton/images.

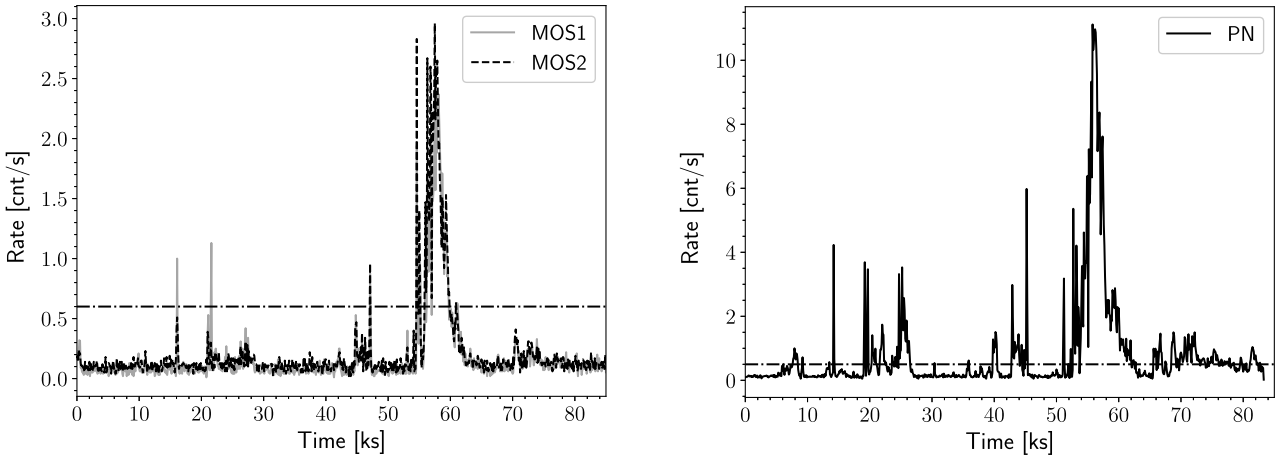

Figure 2. High-energy light curves obtained from the FOVs of MOS (10–12 keV; left-hand panel) and pn (12–14 keV; right-hand panel) detectors. The dash-dotted lines indicate thresholds used to filter out periods of background flares.

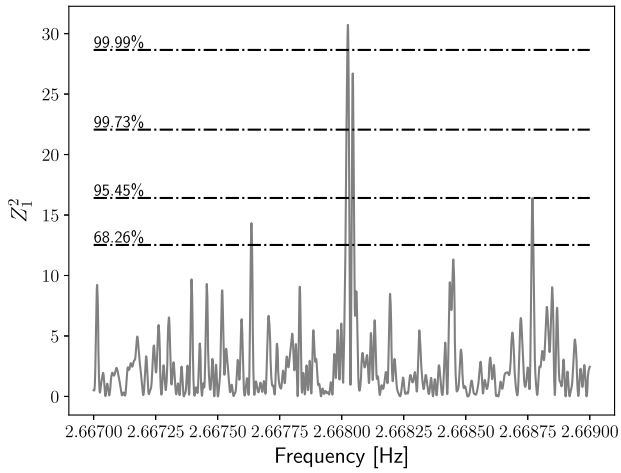

Figure 3. Z_1^2-test periodogram for J1957. The dashed lines show confidence levels.

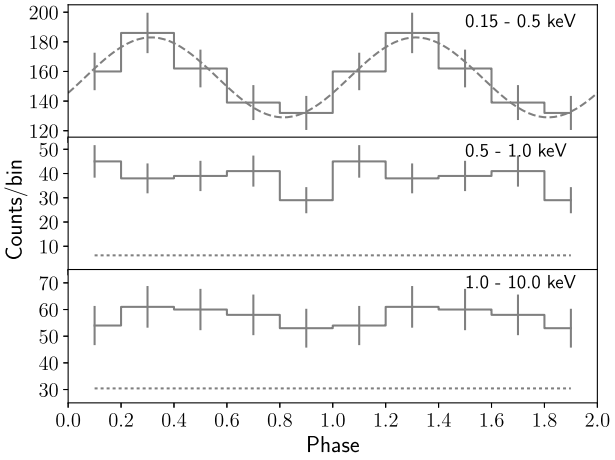

Figure 4. Folded X-ray light curves for J1957 in different energy bands indicated in the panels (periods of background flares are removed). The dotted lines in the middle and bottom panels indicate the background level. In the 0.15–0.5 keV band the background contribution (≈12 counts phase bin^{-1}) is very low in comparison with the pulsar count rate and thus it is not shown. The best-fitting sine curve is overlaid.

command using DE405 ephemeris and the pulsar coordinates derived from the *Chandra* data. We extracted events in the 0.15–0.5 keV band using the 12.5 arcsec radius circle around the *Chandra* position of J1957. Such a small aperture was chosen to eliminate the contribution from the star 'A' located at about 20 arcsec from the pulsar. We searched for pulsations utilizing Z_1^2-test (Buccheri et al. 1983) and 2.667–2.669 Hz frequency range, encapsulating the predicted pulsar rotation frequency of about 2.6680281 Hz obtained from extrapolation of the *Fermi* timing solution to the epoch of the *XMM–Newton* observations (MJD 58761), and with a step of 0.1 μHz.

The resulting periodogram is shown in Fig. 3. The maximum Z_1^2 is ≈ 30.7. This implies the confidence level of a detection $C = [1 - \mathcal{N}\exp(-Z^2_{1,\max}/2)] \times 100$ per cent = 99.996 per cent (or $\approx 4\sigma$) where $\mathcal{N} = \Delta f \times T_{\rm obs}$ is the number of statistically independent trials, Δf is the frequency range and $T_{\rm obs}$ is the duration of the observation. The corresponding frequency is 2.6680249(12) Hz (the frequency 1σ uncertainty was calculated using the formula from Chang et al. 2012). This is consistent within 3σ with the predicted value from *Fermi* timing solution and firmly establishes the pulsar nature of the X-ray source.

The J1957 X-ray pulse profile obtained using the derived frequency is presented in Fig. 4. We see that pulsations are clearly detected only in the very soft band. Non-detection in harder bands is likely due to the low number of counts from the pulsar. The background-corrected pulsed fraction in the 0.15–0.5 keV band PF $= (f_{\max} - f_{\min})/(f_{\max} + f_{\min})$, where $f_{\max}$ and $f_{\min}$ are the maximum and minimum intensity of the folded light curve, is ≈18 ± 6 per cent. As an additional check, we fitted the pulse profile in the 0.15–0.5 keV band with a sine function (fundamental component; see Fig. 4) and got the same result. Following the method from Brazier (1994), we estimated the 99 per cent upper limits on the pulsed fraction of ≈44 per cent in the 0.5–1 keV band and ≈64 per cent in the 1–10 keV band.

4 SPECTRAL ANALYSIS

4.1 J1957

We extracted the time-integrated pulsar spectra from both the *XMM–Newton* and *Chandra* data. In the latter case we utilized

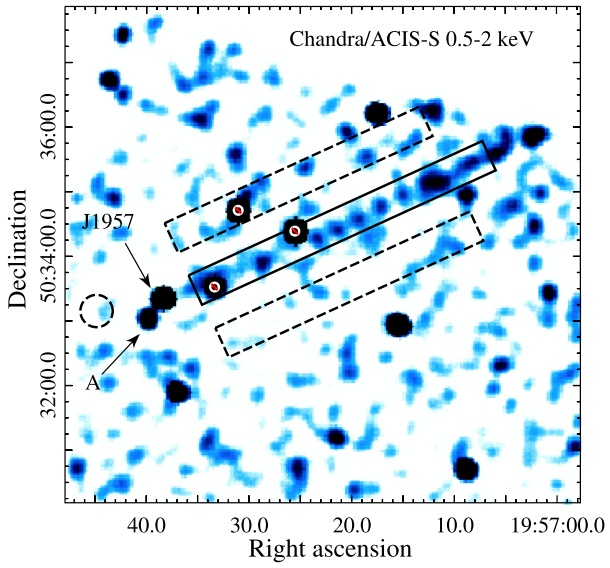

Figure 5. *Chandra* ACIS image of the J1957 field in the 0.5–2 keV band. J1957 and the nearby star 'A' also marked. The background for the pulsar was extracted from the dashed circle. The solid rectangle shows the region used to extract the spectrum of the trail-like nebula while the dashed rectangles were used for the background. Stars excluded from the regions are shown by crossed circles.

the SPECEXTRACT routine and the 2.5-arcsec radius aperture. The *XMM–Newton* spectra were extracted from the 12.5-arcsec radius circle using EVSELECT task and redistribution matrix and ancillary response files were created by RMFGEN and ARFGEN commands. The background spectrum was obtained from the source-free region (see Fig. 5). For the interstellar medium (ISM) absorption, we applied TBABS model with the WILM abundances (Wilms, Allen & McCray 2000). The spectra were fitted simultaneously in the X-Ray Spectral Fitting Package XSPEC v.12.10.1[4] (Arnaud, Gordon & Dorman 2018). We used the following energy ranges: 0.3–10 keV for the *Chandra*, 0.2–10 keV for the MOS and 0.15–10 keV for the pn spectra. The resulting number of source counts after background subtraction is 232(MOS1) + 254(MOS2) + 902(pn) + 88(ACIS).

As a first step, to check how different models fit the data, we applied the χ^2-statistic and grouped the data to ensure 25 counts per energy bin. The single absorbed PL (which describes the pulsar non-thermal emission of magnetospheric origin) or blackbody (BB, which describes the thermal emission from the NS surface) models resulted in unacceptable fits with reduced $\chi^2_\nu = 2.36$ and 5.5 for 54 degrees of freedom (dof), respectively. Then we tried the composite BB + PL model and found that it fits the spectra well with $\chi^2_\nu = 1.13$ (52 dof).

For the thermal component, we also tried the NS magnetized atmosphere models NSMAXG (Ho, Potekhin & Chabrier 2008) presented in the XSPEC package assuming an NS mass $M_{\rm NS} = 1.4\,{\rm M}_\odot$ and radius $R = 13$ km. However, in this case the temperature tends to the lowest value available for these models $\lg(\mathbf{T}/{\rm K}) = \mathbf{5.5}$; here and hereafter $\lg \equiv \log_{10}$. Therefore, we calculated another grid of NS atmosphere models, NSMDIP, which include lower temperatures for the magnetic fields that seem to be likely for this pulsar. We assumed a dipole magnetic field (taking the effects of General Relativity into account) and a corresponding distribution of the local effective temperature over the stellar surface. In these models, the angle α between the rotation and the magnetic axes and the angle ζ between the rotation axis and the line of sight can be used as free parameters. The total thermal luminosity L^∞ that would be measured by a distant observer is calculated by a proper surface integration and converted into the global effective temperature T^∞. The details of calculations are presented in Appendix A.

We have tested several NSMDIP models (Table A1). In model NSMDIP1, we have assumed the canonical NS mass $M = 1.4\,{\rm M}_\odot$ and magnetic field at the pole $B_{\rm p} = 3 \times 10^{12}$ G, which corresponds to the characteristic magnetic field $B \approx 1.65 \times 10^{12}$ G of J1957 at the equator derived from the spin-down. The radius $R = 12.6$ km was taken according to the EoS BSk24 (Pearson et al. 2018); the corresponding gravitational redshift is $z_{\rm g} = 0.22$, and surface gravity $g_{\rm s} = 1.43 \times 10^{14}$ cm s^{-2}. In order to test a higher redshift, we consider a more compact NS model (NSMDIP2) with $M = 2\,{\rm M}_\odot$ and $R = 11.4$ km ($z_{\rm g} = 0.44$ and $g_{\rm s} = 3 \times 10^{14}$ cm s^{-2}), which approximately corresponds to the EoS BSk26. Model NSMDIP3 has the same $z_{\rm g}$ and R as model 1 but a more consistent magnetic field estimate. The canonical characteristic magnetic field is the equatorial field of an orthogonal rotating dipole in vacuum with the given spin period and its derivative, assuming $R = 10$ km and $I_{45} = 1$, where I_{45} is the moment of inertia in units of 10^{45} g cm^2 (e.g. Manchester & Taylor 1977). However, according to the EoS BSk24, for $M = 1.4\,{\rm M}_\odot$ we have $R = 12.6$ km and $I_{45} = 1.51$. Moreover, the spin-down of a pulsar is affected by its magnetosphere. Results of numerical simulations of plasma behaviour in the pulsar magnetosphere suggest that the characteristic magnetic field should be multiplied by a factor of $0.8\,(R/10\ {\rm km})^{-3}\,(1+\sin^2\alpha)^{-1/2}\,\sqrt{I_{45}}$, where α is the angle between rotational and magnetic axes (Spitkovsky 2006). For the abovementioned values of R and I_{45} this implies a 2–3 times weaker field compared to the characteristic one. Thus we adopted $B_{\rm p} = 1.1 \times 10^{12}$ G in model NSMDIP3 which corresponds to the field strength at the equator $B_{\rm eq} \approx 6 \times 10^{11}$ G, that is 2.7 times smaller than the pulsar characteristic (spin-down) field. We find that all three absorbed NSMDIP + PL models describe the data equally well as the BB + PL model giving $\chi^2_\nu \approx 1.17$ (51 dof).

Since the number of source counts is not large, in order to get the most robust estimates of the model parameters and their uncertainties from spectral fits, we regrouped all spectra to ensure at least 1 count per energy bin and therefore used *W*-statistic (Arnaud et al. 2018) which is *C*-statistic (Cash 1979) suitable for Poisson data with Poisson background. We then performed the fitting using a Markov chain Monte Carlo (MCMC) sampling procedure. We employed the affine-invariant MCMC sampler developed by Goodman & Weare (2010) and implemented in a PYTHON package EMCEE by Foreman-Mackey et al. (2013). In addition, to estimate the distance to J1957, we used the interstellar absorption–distance relation towards the pulsar as a prior (see Appendix B for details). About 100 walkers and 13 000 steps were typically enough to ensure fit convergences. Using the sampled posterior distribution, we obtained the best-fitting parameters of the models with uncertainties, which are defined as their maximal-probability density values and respective credible intervals.

In the case of NSMDIP + PL models, we found that our data are rather insensitive to the α and ζ angles. From Fig. 4, one can see that there is one pulse per period. This implies that $\alpha + \zeta \leq 90^\circ$, which was used as a prior in the spectral fitting. As an example, 1D and 2D marginal posterior parameter distribution functions for the NSMDIP1 + PL model are shown in Fig. 6. One can see that the angles, in contrast to other parameters, cannot be well constrained from the fit.

[4] https://heasarc.gsfc.nasa.gov/docs/xanadu/xspec/

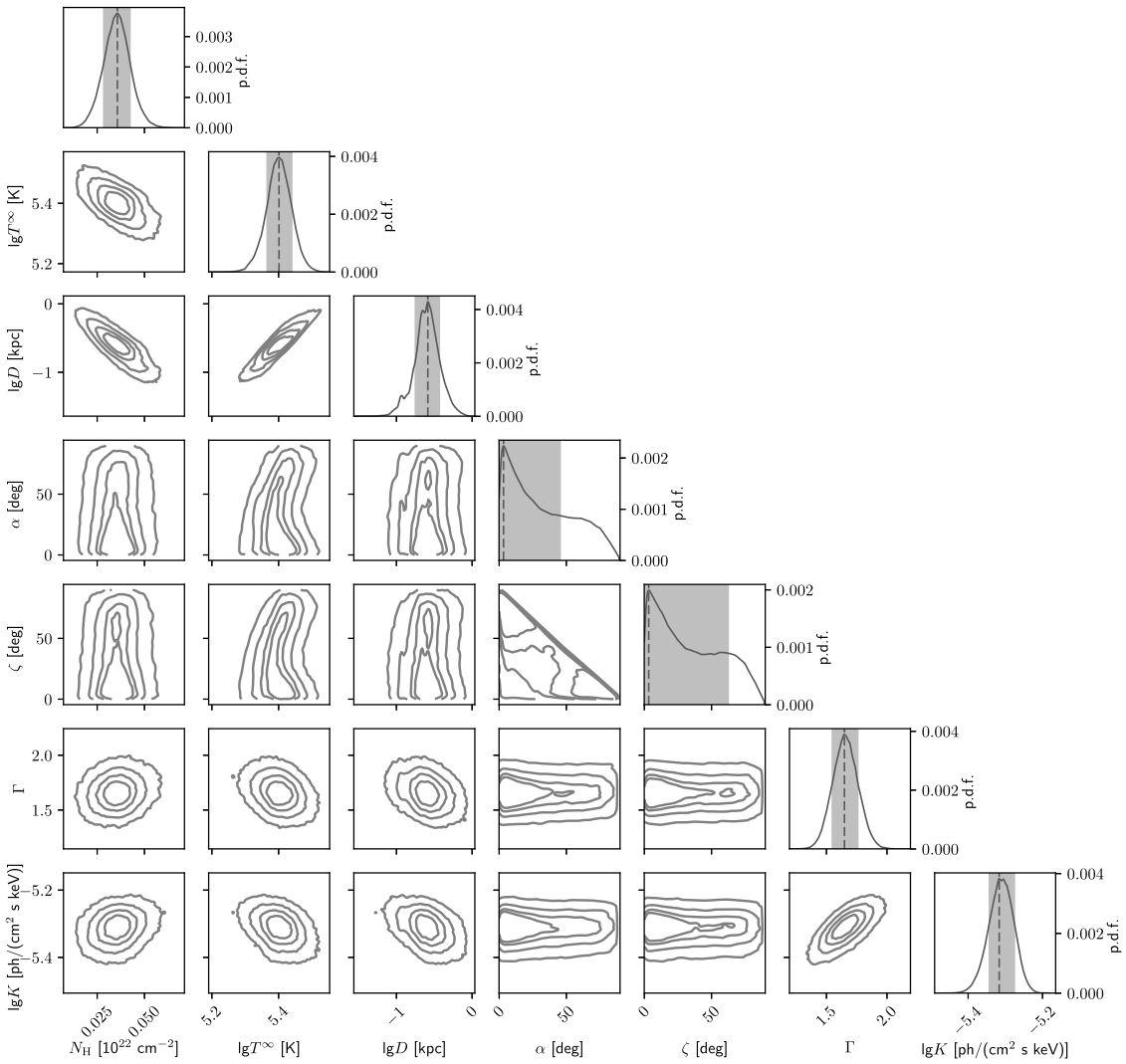

Figure 6. 1D and 2D marginal posterior distribution functions (p.d.f.) for parameters of the NSMDIP1 + PL model (see Table 1). The vertical dashed lines in 1D distributions indicate the best-fitting values while light grey strips show 1σ credible intervals. In 2D distributions, 40, 68, 90, and 99 per cent confidence contours are shown.

Their formal best-fitting values are close to 0°. Our fits show that the similar situation occurs for the NSMDIP2 + PL and NSMDIP3 + PL models. However, for any of the models the probability density function for angles remains relatively high for the whole meaningful ranges of 0°– 90°. This results in a very large formal uncertainties of the angles, and in fact they can accept any value. For these reasons, angles are not included in the parameter list of Table 1 presenting the fit results. We found that other fit parameters depend on a specific value of angles only weakly. We also fitted spectra using two models of the J1957 γ-ray emission geometry, polar cap (PC), and slot-gap (SG), obtained from the *Fermi* data by Pierbattista et al. (2015) which satisfy the condition $\alpha + \zeta \leq 90°$.[5] The results for the SG with $\alpha = 66°$ and $\zeta = 24°$ are presented in Table 2 and Fig. 7. This model geometry is more preferable as it gives an acceptable X-ray pulse shape and pulsed fraction (see Section 5 for details).

To understand which of the models is statistically more preferable, Tables 1 and 2 also present a Bayesian evidence $\mathcal{L}$ and information criteria BIC $= n \ln N_{\rm b} - 2 \ln \mathcal{L}$, where n is the number of free model parameters and $N_{\rm b}$ is the number of spectral bins (which is 373). When picking from several models, the one with the lowest BIC is preferred. As seen, the BB + PL model has the smallest BIC and appears to be preferable. The strength of the evidence against NSMDIP + PL models with the higher BICs is defined by $\Delta{\rm BIC} \gtrsim 15$ for atmosphere models with free angles which is evaluated as a very strong evidence. At the same time, ΔBICs for any pair of NSMDIP + PL models in Table 1 is $\lesssim 2$, which is qualified either as weakly

[5]Pierbattista et al. (2015) used polar cap (PC), slot gap (SG), outer gap (OG), and one pole caustic (OPC) models which assume different regions of the pulsar magnetosphere where particles are accelerated and emit γ-rays. In the PC model this occurs at low altitudes near the magnetic poles and in the SG model – in a slot gap, which is a narrow gap extending from the polar cap surface to the light cylinder. In the OG model the gap extends from the null charge surface to high altitudes along the last-open-field lines. The OPC is a variation of the OG model which suggests different gap width and energetics. The SG and OG can provide wide γ-ray beams and imply exponential spectral cut-off at high energies while the PC provides narrow beams and predicts super-exponential spectral cut-off due to magnetic pair production process.

Table 1. Best-fitting parameters for different models with thawed α and ζ angles and accounting for $\alpha + \zeta <= 90^\circ$.

Model	$N_{\rm H}$, 10^{20} cm^{-2}	$k_{\rm B}T^\infty$, eV	R^∞, km	lg L^∞, erg s^{-1}	Γ	K, ph cm^{-2} s^{-1} keV^{-1}	D, pc	$-\ln\mathcal{L}$	BIC
BB + PL	$2.2^{+1.6}_{-1.0}$	54^{+5}_{-7}	$2.2^{+5.0}_{-2.0}$	$30.66^{+0.85}_{-1.72}$	$1.76^{+0.11}_{-0.11}$	$5.4^{+0.4}_{-0.4}\times10^{-6}$	545^{+463}_{-445}	193.5	416.6
NSMDIP1 + PL	$3.6^{+0.6}_{-0.5}$	$21.7^{+2.0}_{-1.7}$	15.4^f	$30.83^{+0.16}_{-0.14}$	$1.65^{+0.11}_{-0.10}$	$4.8^{+0.5}_{-0.3}\times10^{-6}$	260^{+109}_{-82}	195.3	432
NSMDIP2 + PL	$3.2^{+0.6}_{-0.7}$	$19.8^{+2.0}_{-1.8}$	16.4^f	$30.72^{+0.17}_{-0.16}$	$1.66^{+0.10}_{-0.11}$	$4.9^{+0.4}_{-0.4}\times10^{-6}$	218^{+164}_{-64}	195.9	433
NSMDIP3 + PL	$2.6^{+0.8}_{-0.5}$	$18.4^{+2.1}_{-2.0}$	15.4^f	$30.55^{+0.19}_{-0.21}$	$1.64^{+0.10}_{-0.10}$	$4.9^{+0.3}_{-0.4}\times10^{-6}$	210^{+108}_{-106}	196.1	433.7

Notes. $^\dagger N_{\rm H}$ is the absorbing column density, $T^\infty = T/(1+z_{\rm g})$ is the effective temperature as measured by a distant observer, $R^\infty = R(1+z_{\rm g})$ is the radius of the equivalent emitting sphere as seen by a distant observer, $L^\infty = L/(1+z_{\rm g})^2 = 4\pi R^2\sigma_{\rm SB}T^4/(1+z_{\rm g})^2$ is the bolometric thermal luminosity as measured by a distant observer ($\sigma_{\rm SB}$ is the Stefan-Boltzmann constant), Γ is the photon index, K is the PL normalization, and D is the distance. For the gravitational redshift $z_{\rm g}$ and unredshifted radius R, see Table A1. The last two columns give the values of the maximum log-likelihood $\ln\mathcal{L}$ and the Bayesian information criterion (BIC). All errors are at 1σ credible interval.
^{f} Fixed parameters.

Table 2. The same as in Table 1 but for fixed angles at $\alpha = 66^\circ$ and $\zeta = 24^\circ$ †.

Model	$N_{\rm H}$, 10^{20} cm^{-2}	$k_{\rm B}T^\infty$, eV	R^∞, km	lg L^∞, erg s^{-1}	Γ	K, ph cm^{-2} s^{-1} keV^{-1}	D, pc	$-\ln\mathcal{L}$	BIC
NSMDIP1 + PL	$3.5^{+0.7}_{-0.6}$	$21.9^{+1.9}_{-1.1}$	15.4^f	$30.85^{+0.14}_{-0.09}$	$1.66^{+0.10}_{-0.11}$	$4.9^{+0.4}_{-0.4}\times10^{-6}$	263^{+112}_{-78}	195.1	419.8
NSMDIP2 + PL	$3.3^{+0.6}_{-0.8}$	$20.3^{+2.0}_{-1.5}$	16.4^f	$30.77^{+0.16}_{-0.14}$	$1.64^{+0.11}_{-0.09}$	$5.0^{+0.3}_{-0.5}\times10^{-6}$	224^{+165}_{-63}	195.7	421.0
NSMDIP3 + PL	$2.9^{+0.5}_{-0.7}$	$19.8^{+1.5}_{-2.6}$	15.4^f	$30.67^{+0.13}_{-0.24}$	$1.63^{+0.11}_{-0.10}$	$4.8^{+0.3}_{-0.4}\times10^{-6}$	212^{+99}_{-110}	195.9	422.2

Note. †Notations are the same as in Table 1.

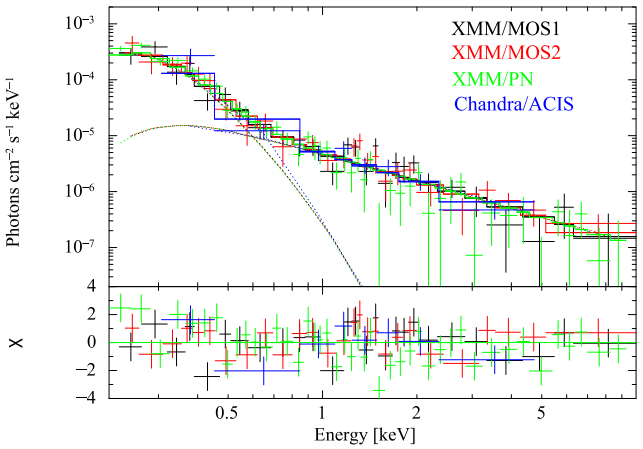

Figure 7. The J1957 unfolded spectrum and the model NSMDIP1 + PL with fixed angles at $\alpha = 66^\circ$ and $\zeta = 24^\circ$ (see the first line in Table 2). The dotted lines show the model components. Data from different instruments are indicated by different colours as indicated in the panel. Spectra were grouped to ensure at least 10 counts per energy bin for illustrative purposes.

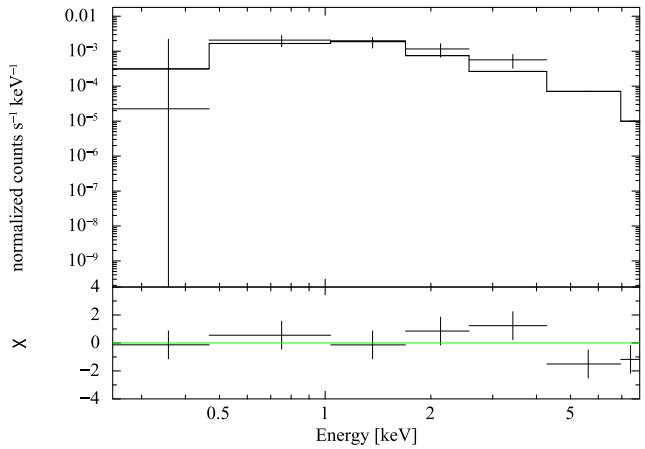

Figure 8. *Chandra* spectrum of the trail-like nebula, the best-fitting PL model and residuals.

positive or not worth more than a bare mention. On the other hand, fixing of α and ζ almost does not change $\mathcal{L}$ while BICs values become smaller. In this case, the difference between NSMDIP + PL and BB + PL models $\Delta{\rm BIC}\lesssim 6$ which changes the strength of evidence from very strong to decisive. Moreover, the models NSMDIP + PL are preferred from the physics point of view, because they assume the plausible NS radii and temperature distributions, whereas the BB + PL model results in a best-fitting radius incompatible with thermal emission from the entire NS surface (see the discussion in Section 5).

4.2 The trail-like nebula

For the spectral analysis of the trail-like nebula, we used only the *Chandra* data set since in the *XMM–Newton* data it is somewhat blurred with several stars. We extracted spectrum of the trail using the 30×300 arcsec^2 rectangle region shown in Fig. 5 together with the regions used for the background. It was binned to ensure at least 25 counts per energy bin and fitted in the 0.3–10 keV band. The total number of counts in the spectrum is 811 while only 105 of them come from the source. We tried the PL model and found that the column density is highly uncertain. Thus, we fixed it at 3×10^{20} cm^{-2} which is compatible with all pulsar models (see Table 1). The resulting parameters $\Gamma = 1.9\pm0.5$, $K = 7.3^{+1.9}_{-1.8}\times10^{-6}$ ph cm^{-2} s^{-1} keV^{-1}, the unabsorbed flux in the 0.3–10 keV band $F_X = 4.5^{+1.6}_{-1.1}\times10^{-14}$ erg s^{-1} cm^{-2} and $\chi^2_\nu = 1.17$ (dof = 29).

Such spectrum can have a synchrotron nature. The spectrum and the best-fitting model are shown in Fig. 8. The spectrum can also be equally well described ($\chi^2_\nu = 1.16$, dof = 29) by the thermal bremsstrahlung model with a temperature $3.6^{+12.1}_{-1.9}$ keV and the unabsorbed flux in the 0.3–10 keV band $F_X = 3.7^{+1.8}_{-1.1}\times10^{-14}$ erg s^{-1} cm^{-2}.

5 DISCUSSION

5.1 The pulsar spectral and timing properties

The time-integrated X-ray spectrum of J1957 the in 0.15–10 keV range can be well described by the composite model consisting of the thermal and PL components while the single PL model suggested previously by Marelli et al. (2015) for a more narrow range of 0.3–10 keV is statistically unacceptable in the extended range. In the case of the BB + PL model, the obtained effective temperature $T^{\infty} \approx 54$ eV (6.3×10^5 K) is typical for the emission from the bulk of an NS surface but the radius of the emitting area is smaller than an expected NS radius of 10–15 km (see Table 1). The thermal emission could be produced by hot polar caps of the NS heated by relativistic particles from pulsar magnetosphere. For J1957, the 'standard' pulsar polar cap radius is about 0.3 km (Sturrock 1971) which is compatible with the lower bound of the derived radius. However, the derived temperature is too low for the polar cap emission (cf. Potekhin et al. 2020), rejecting this possibility. Thus, the BB + PL model might describe some hotter part of the pulsar surface while the other part is cooler and not observed in X-rays as takes place, e.g. for the middle-aged PSR B1055−52 (Mignani, Pavlov & Kargaltsev 2010). Note, however, that such interpretation implies that the obtained BB temperature cannot be used for a comparison with the predictions of the cooling theory; instead, the bolometric thermal luminosity should be used for such a comparison (as discussed, e.g. in Potekhin et al. 2020). Remarkably, the best-fitting thermal luminosities given by the BB + PL and NSMDIP + PL models are compatible within uncertainties (see Table 1).

The NSMDIP + PL models also give acceptable fits. Although they are possibly less preferable according to the Bayesian criteria that disregard prior theoretical constraints on NS radii, they are more physically motivated. In particular, they are based on the magnetic atmosphere models, computed for realistic NS parameters, and they consistently take into account the distributions of temperature and magnetic field over the NS surface. Combining the results from all these models (Table 1), the estimated redshifted NS effective temperature $T^{\infty} \approx 20 \pm 4$ eV (0.23 ± 0.05 MK). This makes the pulsar one of the coldest among all known NSs with estimated thermal luminosities, whose measured thermal emission from the surface is powered by cooling (see Section 5.3). We cannot constrain the pulsar viewing geometry (angles α and ζ) from the time-integrated spectra.

For the first time, we detected X-ray pulsations with the pulsar spin period. The pulsations are significant only in the soft band of 0.15–0.5 keV where the thermal emission component strongly dominates in the spectrum of the pulsar. The pulse profile is a sine-like with a single pulse per period and the pulsed fraction of $\approx 18 \pm 6$ per cent, which is typical for thermal emission from a bulk of the surface of NSs (e.g. Pavlov & Zavlin 2000a; Zavlin 2009). This is independent confirmation of the results of the spectral analysis. The pulsations can be due to non-uniform temperature distribution over the surface of the NS due to magnetic anisotropy of the internal heat transfer to the star surface and the magnetic beaming of the radiation in its atmosphere. Both factors are accounted in our NSMDIP models, while only the first one can provide pulsations for the BB model which may be reminiscent of the emission from a solid state surface of the NS. In any case, using the BB model with a single temperature is a very rude simplification at the non-uniform temperature distribution over the star surface.

The observed soft X-ray pulsations can be used to constrain the angles α and ζ that the rotation axis makes with the magnetic axis and the line of sight (magnetic obliquity and pulsar inclination), assuming that the flux in the photon energy band 0.15–0.5 keV is dominated by thermal emission. In the left-hand panel of Fig. 9, the hatched regions correspond to the α and ζ values that provide the observed pulsed fractions of thermal radiation from 0.12 to 0.24 in the 0.15–0.5 keV energy band for the atmosphere models NSMDIP 1–3, according to the legend. We see that for all the considered cases $\alpha + \zeta \gtrsim 30^{\circ}$. Because of a higher redshift in model NSMDIP 2, it shows a stronger gravitational light bending, which leads to a stronger smearing of the light curves, compared with the two other models. Therefore, higher α and ζ are needed to obtain the same pulsed fraction. In particular, the upper limit of 24 per cent is never reached (that is why the hatched area has a shape of a bell rather than a horseshoe in this case). The absence of an interpulse on the observed light curve in Fig. 4 suggests that $\alpha + \zeta \lesssim 90^{\circ}$. The curves in Fig. 9, left, show the combinations of α and ζ that provide the pulsed fraction 18 per cent. For comparison, we show an analogous line for the best-fitting BB model from Table 1 ($R^{\infty} = 2.2$ km), assuming that thermal radiation comes from two uniformly heated circular regions around the poles on the surface of a star with the same $M = 1.4$ M$_{\odot}$ and $R = 12.6$ km as in models NSMDIP 1 and 3. In contrast to the atmosphere radiation, which is has a peaked angular distribution, the BB radiation obeys the Lambert's cosine law. For this reason, the same pulsed fraction is reached for higher $\alpha + \zeta$ values. For NSMDIP 2, the abovementioned smearing of the light curves due to the light bending effect is so strong that the pulsed fraction does not exceed 5 per cent, meaning that the BB model is inapplicable in this case. We also show the tentative α and ζ values obtained by Pierbattista et al. (2015), who fitted geometrical models to the observed γ-ray pulse profile, using different theoretical models of γ-ray pulse formation. We see that one of the models (the slot gap model) is compatible with NSMDIP 1 and NSMDIP 2. Examples of theoretical light curves, calculated as described in Appendix A, are shown in the right-hand panel of Fig. 9. For each model we show three cases, marked by letters A, B, and C, corresponding to the magnetic obliquity α and inclination ζ values shown in the left-hand panel. Note, that case C does not agree with the observed profile since it predicts the presence of an interpulse and thus can be excluded.

The low number of counts does not allow us to perform the phase-resolved spectral analysis which could help us to distinguish between different geometries and spectral models. Deeper X-ray observations are necessary to do that. Ultraviolet (UV) observations could also clarify the situation whether the thermal emission is best described by the NSMDIP or by the BB (solid state) spectral models as they predict different fluxes in this range.

Implementation of the extinction–distance relation in the fitting procedure allowed us to estimate the distance to J1957. We note, that due to the large relative uncertainties in this relation especially at low distances (see Appendix B), the constraints on D are rather weak especially for the BB + PL model where $N_{\rm H}$ uncertainties are larger than for the atmosphere models. Thus, the BB + PL model gives the distance up to $\approx$1 kpc while the NSMDIP + PL models resulted in the range of 0.1–0.4 kpc. The former estimate is compatible with the 'pseudo'-distance of 0.8 kpc (Marelli et al. 2015). Note, that the obtained distance range gives a reasonable γ-ray efficiency $\eta_{\gamma} = L_{\gamma}/\dot{E}$ of $\approx$0.006–0.6 where $L_{\gamma} = 4\pi D^2 G_{100}$ is the γ-ray luminosity and $G_{100} = 2.6 \times 10^{-11}$ erg s^{-1} cm^{-2} (Marelli et al. 2015) is the γ-ray flux above 100 MeV.

As for the PL spectral component, the derived photon index range of 1.5–1.9 is typical for pulsars (e.g. Kargaltsev & Pavlov 2008). For all the models, the unabsorbed non-thermal flux in the 2–10 keV band is $F_X \approx 2 \times 10^{-14}$ erg s^{-1} cm^{-2}. This corresponds to X-ray luminosity L_X of $\approx$(0.24–3.83) $\times$ 10^{29} erg s^{-1} for the distance range of 100–

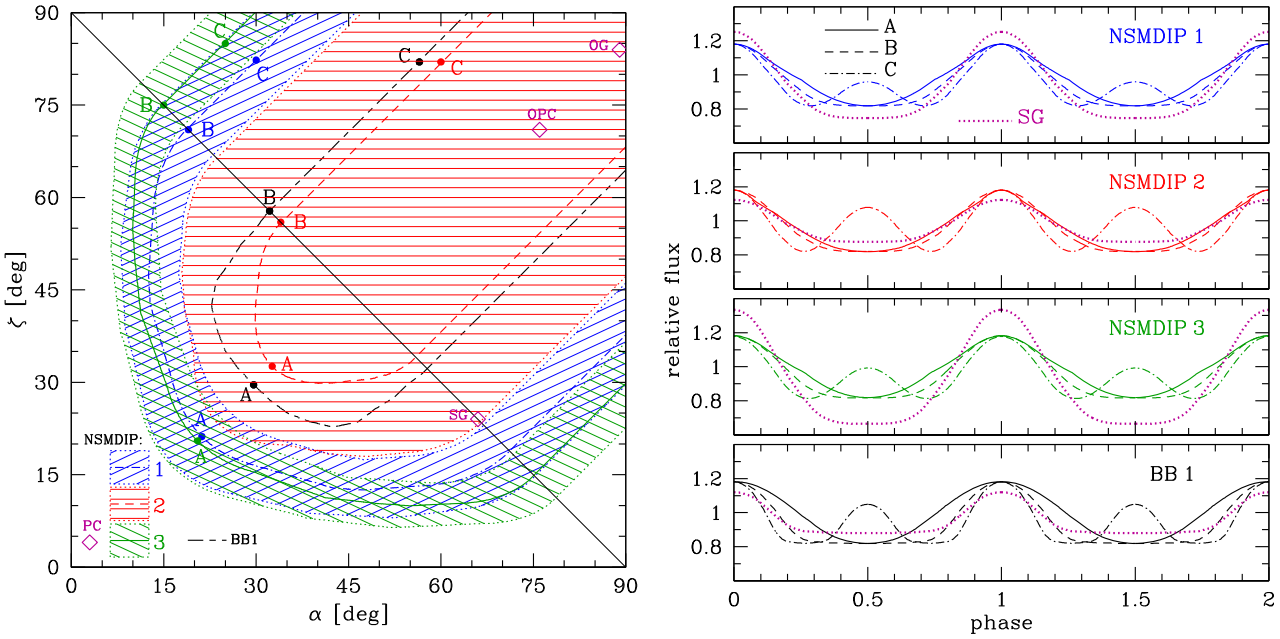

Figure 9. Left-hand panel: Regions of magnetic obliquity α and rotation axis inclination ζ (hatched regions), compatible with the observed pulsed fraction 0.18 ± 0.06 of emission in the soft X-ray energy band 0.15–0.5 keV, and the α and ζ combinations (curves) that provide the pulsed fraction 0.18, shown for the three NSMDIP atmosphere models according to the legend. For comparison, a curve for a BB model (see the text) is also plotted. The diagonal line separates the parts of the hatched regions in the lower triangle, which are compatible with the singe-pulsed light curves, as observed in Fig. 4. The violet diamonds show the tentative α and ζ values obtained by Pierbattista et al. (2015) using polar cap (PC), slot gap (SG), outer gap (OG), and one pole caustic (OPC) models of gamma-ray pulse formation. Right-hand panel: Light curves in the redshifted energy band 0.15–0.5 keV, computed for models NSMDIP 1, 2, and 3 at $\lg T^{\infty}(\mathrm{K}) = 5.4$ (the three upper panels) and the α and ζ angles shown by the respective points A, B, and C in the left-hand panel (solid, dashed, and dot-dashed lines). For comparison, the bottom panel shows the light curves computed for the best-fitting BB model. The violet dotted line in each panel shows the light curve for $\alpha = 66^{\circ}$ and $\zeta = 24^{\circ}$ given by the fit with the SG model (Pierbattista et al. 2015).

400 pc provided by the atmosphere models and up to 2.4×10^{30} erg s^{-1}erg s^{-1} with the upper bound on the distance of 1 kpc as provided by the BB model. The corresponding X-ray efficiency of $\eta_X = L_X/\dot{E} = 10^{-5.34} - 10^{-4.14}$ and up to $10^{-3.35}$, respectively. These values are compatible with empirical dependencies of pulsar X-ray non-thermal luminosity and efficiency versus characteristic age (see e.g. Zharikov, Shibanov & Komarova 2006; Zharikov & Mignani 2013). Upper limits on the pulsed fraction in harder bands of ≈40–60 per cent do not give any additional informative constraints on the properties of the non-thermal X-ray emission from the pulsar magnetosphere.

5.2 The nature of the trail-like nebula

As was noted in Section 2, there is a thin straight feature protruding north-west from the pulsar (in equatorial coordinates; Fig. 5) likely associated with it. Its spectrum can be well described by the PL model with parameters typical for X-ray synchrotron nebulae powered by pulsars, known as PWNe. Its length is ≈8 arcmin which corresponds to ≈0.23–2.3 pc for the obtained distance range of 0.1–1 kpc (see Table 1). This is compatible with lengths of other PWNe (e.g. Kargaltsev et al. 2017).

We can assume that the J1957 moves in the southeast direction and thus the feature is a trail-like PWN as observed e.g. for PSR J1741–2054 (Auchettl et al. 2015). On the other hand, this can be a misaligned outflow which is not aligned with the pulsars's proper motion (p.m.) direction (see e.g. Reynolds et al. 2017; Kargaltsev et al. 2017, and references therein). If so, we do not see any hint of a 'normal' tail-like PWN protruding behind the pulsar in X-ray images. Torus or jet structures typical for PWNe of younger pulsars are also not detected. However, the situation can be similar to the Guitar nebula powered by PSR B2224+65: the guitar-shaped bow-shock nebula was detected in Hα while no head-tail PWN was found within the shock in X-rays (Reynolds et al. 2017). Instead, X-ray observations revealed a jet-like feature inclined by ≈118° to the p.m. direction of B2224+65. For our pulsar, no Hα emission was detected around it with the 3.6 m WIYN telescope at a 300 s exposure (Brownsberger & Romani 2014). However, the exposure may be too short to detect a fainter bow-shock at a high Galactic latitude of ≈11° where the density of the interstellar matter is small and deeper observations are needed.

The tail interpretation suggests that J1957 should move towards the Galactic plane (Fig. 1) raising a question about its birth site somewhere in the Galactic halo. For the misaligned outflow, the direction of p.m. remains unclear. In the latter case, we can assume that J1957 was born in the Galactic disc since this possibility is more plausible than the birth in the halo. Due to the natal kick in the supernova explosion it could achieve high velocities and move away from the disc. In such a case, we can estimate the J1957 p.m. perpendicular to the Galactic plane. At the pulsar Galactic latitude of ≈11° the p.m. $\mu \approx 47\, t_{840\ \mathrm{kyr}}^{-1}$ mas yr^{-1}, where $t_{840\,\mathrm{kyr}}$ is the pulsar true age normalized to its characteristic age t_c. This corresponds to the transverse velocity $v \approx 220\, t_{840\ \mathrm{kyr}}^{-1} D_{\mathrm{kpc}}$ km s^{-1} which is compatible with the pulsars velocity distribution (Hobbs et al. 2005) for the estimated distance range even if the true age is ∼5 times smaller.

The nebula spectrum can be also described by a thermal bremsstrahlung emission model with a temperature of $3.6^{+12.1}_{-1.9}$ keV. In this case the nebula emission comes from the shocked ISM

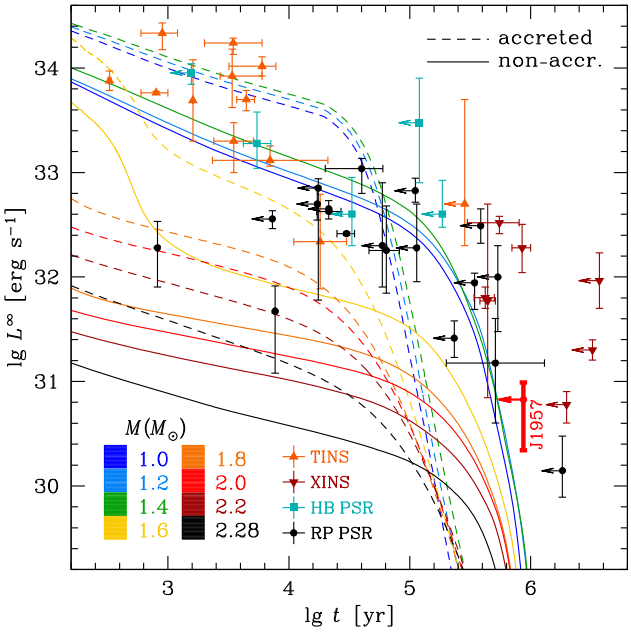

Figure 10. Cooling curves of NSs with different masses (coded with colour), described by the EoS BSk24, for accreted and non-accreted heat blanketing envelopes, compared with observations. The data are plotted as indicated in the legend for NS classes following Potekhin et al. (2020): weakly magnetized thermally emitting isolated NSs (TINS), X-ray isolated NSs (XINS), high-B pulsars (HB PSRs), and rotation powered ('ordinary') pulsars (RP PSR). The vertical error bars show the estimated uncertainties on bolometric thermal luminosities, as seen by a distant observer. The horizontal error bars show the estimated age intervals, whenever available; otherwise horizontal arrows mark the characteristic ages (which are usually, although not always, larger than the true ages). The position of J1957 in this figure corresponds to the best-fitting model NSMDIP 1, while the error bar embraces the models NSMDIP 1–3 in Table 1.

and the pulsar p.m. must be aligned with the nebula axis. Such situation appears for the tail of PSR J0357+3205 (Marelli et al. 2013). However, due to low count statistics it is hard to distinguish between the PL and the thermal models in our case.

Measurement of the pulsar's p.m. is necessary to understand the nature of the feature and deeper X-ray observations are needed to constrain its shape and spectral properties.

5.3 J1957 and the cooling theory

As noted above, J1957 can be one of the coldest cooling NSs with measured surface temperatures (e.g. Potekhin et al. 2020 and references therein). In Fig. 10 we compare the estimated thermal luminosities of different isolated NSs with theoretical cooling curves (i.e. redshifted luminosities as functions of ages). For J1957 we use the luminosity estimates reported in Table 1. The error bar unites the uncertainties for the models NSMDIP 1–3. The model NSMDIP 1 is adopted as the best estimate, because it provides the lowest BIC value among these three models. The observational estimates for the other cooling NSs are taken from Potekhin et al. (2020).[6] For the NSs lacking timing-independent age estimates, including J1957, we plot L^∞ against their characteristic ages t_c. In these cases the leftward arrows indicate that t_c is likely to be larger than the true age, which is the common case, although there are exceptions where t_c is somewhat lower than the true age (see, e.g. examples, discussion and references in Potekhin et al. 2020). We see that J1957 has the lowest thermal luminosity among all cooling NSs with ages <1 Myr.

The theoretical cooling curves in Fig. 10 are calculated using the numerical code presented by Potekhin & Chabrier (2018). The BSk24 model (Pearson et al. 2018) is used for the composition and EoSp of the NS matter. The NSs are supposed to have either non-accreted (ground state) heat blanketing envelopes or accreted envelopes composed of helium, carbon, and oxygen up to the densities and temperatures where these chemical elements can survive (see e.g. Potekhin et al. 2003; Potekhin & Chabrier 2018). The accreted envelopes are more heat-transparent than the ground-state ones. For this reason, the stars with the accreted envelopes are brighter at the early stage of their evolution (at $t \lesssim 10^4$ yr), but they cool down faster and become colder at the late stage ($t \gtrsim 10^5$ yr). An envelope may consist of the accreted material only partially. In such cases the cooling rate is intermediate between the non-accreted and fully accreted extremes shown in the figure.

The critical temperatures for singlet neutron superfluidity in the inner crust and for proton and triplet neutron types of superfluidity in the core of an NS are evaluated, as functions of density, using the MSH, BS, and TTav parametrizations of Ho et al. (2015), which are based on theoretical models computed, respectively, by Margueron, Sagawa & Hagino (2008), Baldo & Schulze (2007), and Takatsuka & Tamagaki (2004). As can be seen from Fig. 10, thermal luminosity of J1957 is higher than the predictions of the cooling model for the age $t = t_c$, so that theoretical cooling curves pass to the left of the error bar in this figure. However, as we mentioned above, it is likely that the true age t is smaller than t_c. If we treat t_c as an upper limit to the true age, than thermal luminosity of J1957 is compatible with the considered theoretical model. The smallest discrepancy between the best-fitting point and the theoretical cooling curves in Fig. 10 is observed for the model of an NS with $M \approx 1.4$ M$_\odot$, covered by the non-accreted heat-blanketing envelope. In this case, an agreement between the model and observations is reached, if we assume that $t \sim 0.5$ Myr $\sim 0.6 t_c$.

However, the cooling NS models shown in Fig. 10, being non-magnetic, are not fully consistent with the models of strongly magnetized atmosphere spectra (Appendix A). To produce cooling curves fully consistent with the spectral fitting, we employ a model of magnetized heat-blanketing envelope with mass 10^{-5} M$_\odot$. The bottom of such an envelope lies in a deep layer of the outer crust (at densities $\sim 10^{11}$ g cm^{-3}), which is nearly isothermal at the considered NS ages. The interior of an NS is treated as spherically symmetric, but temperature distribution in the envelope is essentially anisotropic. At the magnetic pole, the mechanical and thermal structure of the envelope is computed numerically, following Potekhin et al. (2003) and using updated microphysics input as per Potekhin & Chabrier (2018). Thermal conductivity treatment in the partially degenerate H and He layers of the accreted envelope has been updated following Blouin et al. (2020). The distribution of the effective temperature over the surface is then taken consistent with the dipole field, including the effects of General Relativity, as described in Appendix A. The interior of the star at densities $\gtrsim 10^{11}$ g cm^{-3} is treated as spherically symmetric, with the microphysics (in particular, thermal conductivities, synchrotron neutrino emission rates, etc.) pertinent to the *average* magnetic field strength for each model. In the cases NSMDIP 1 and 3 ($M = 1.4$ M$_\odot$), we use the composition and EoS model BSk24, while for NSMDIP 2 we use BSk26 (Pearson et al. 2018). The latter EoS is softer and provides the core composition preventing neutron star from the enhanced cooling at the assumed redshift $z_g = 0.44$, which corresponds to $M \approx 2$ M$_\odot$.

[6] http://www.ioffe.ru/astro/NSG/thermal/cooldat.html

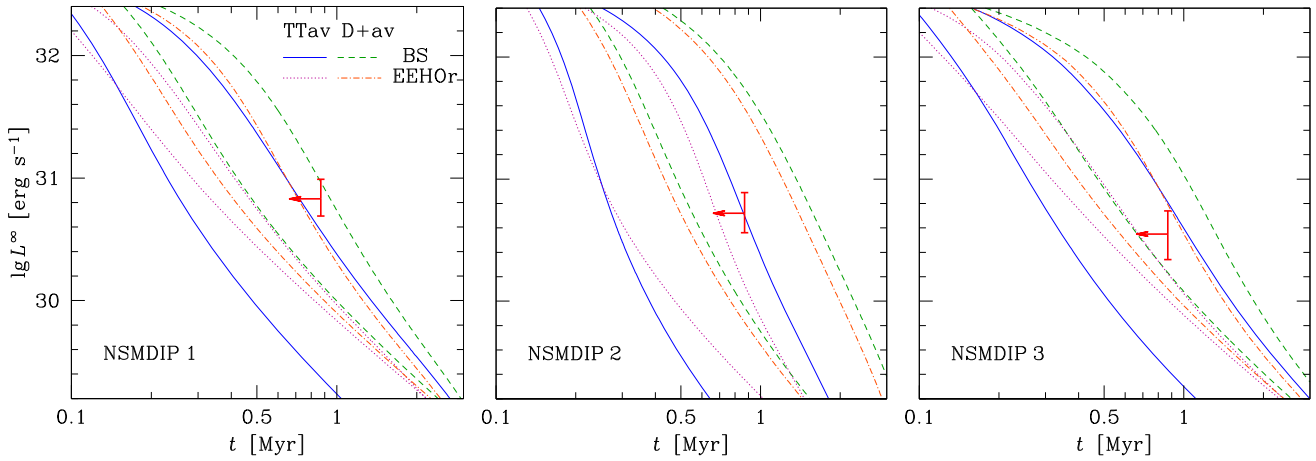

Figure 11. Late-time cooling of a strongly magnetized NS, consistent with the spectral fit models NSMDIP 1, 2, and 3 (the left-hand, middle, and right-hand panels, respectively). The EoS model BSk24 with $M = 1.4$ M$_\odot$ is used for NSMDIP 1 and 3, and BSk26 with $M = 2$ M$_\odot$ is used for NSMDIP 2. The polar magnetic field is $B_p = 3 \times 10^{12}$ G (average $\langle B\rangle = 2.2 \times 10^{12}$ G) for NSMDIP 1 and 2, while for NSMDIP 3 we adopt $B_p = 1.1 \times 10^{12}$ G ($\langle B\rangle = 7.9 \times 10^{11}$ G). Different line styles correspond to different models of baryon superfluidity in the stellar core, as shown in the legend: BS or EEHOr models for the proton pairing gap and TTav or D+av models for the neutron triplet pairing (see the text). In each panel, the right/upper line of each type shows the cooling of an NS covered by a non-accreted magnetized heat blanket made of iron, while the left/lower line of each type corresponds to the fully accreted heat-blanketing envelope composed of layers of hydrogen, helium, carbon, and oxygen (Potekhin et al. 2003; Potekhin & Chabrier 2018).

The results are shown in Fig. 11. To test the effects of baryon superfluidity we show, in addition to the models with the BS and TTav superfluidity of protons and neutrons (as in Fig. 10), also the cooling curves computed using alternative proton and neutron superfluidity models in the core. For an alternative proton superfluidity, we use the EEHOr parametrization by Ho et al. (2015) to the microscopic calculations of proton critical temperature by Elgarøy et al. (1996), which predicted substantially stronger proton superfluidity than BS. For an alternative superfluidity of neutrons, we use the 'Av18 SRC+P' model of Ding et al. (2016). which is marked 'D+av' in Fig. 11. In the latter case, the triplet neutron superfluidity is suppressed due to the effects of many-body correlations (although the maximum critical temperatures are similar in the TTav and D+av models, the latter model predicts a narrower range of densities where the neutrons are superfluid).

We see that the obtained estimates of thermal luminosity of J1957 can constrain the theoretical NS cooling models, constructed consistently with the fitting. Assuming that the true age of the pulsar does not exceed its characteristic age, we can conclude that the NS model NSMDIP 1 is compatible with all employed models of superfluidity and envelope composition, but the NS models NSMDIP 2 and 3 are hardly compatible with the suppressed neutron superfluidity (D+av), if the envelope is non-accreted. If we assume that the true age is close to t_c, then for each spectral model we can select the best-fitting superfluidity and heat-blanketing envelope models in Fig. 11, for which the cooling curves are in a good agreement with the spectral fitting results. This reinforces the suggestion that the thermal-like part of the X-ray radiation of J1957 comes from the entire surface and is powered by passive cooling. Large uncertainties of the thermal luminosity provided by the BB model do not allow us to constrain cooling models.

6 SUMMARY

Using the *XMM–Newton* and *Chandra* observations of the middle-aged γ-ray pulsar J1957, we detected, for the first time, the thermal spectral component and X-ray pulsations. We performed self-consistent modelling of thermal spectrum and cooling for models of NSs with strong dipole magnetic field. We applied it to the observations and estimated the J1957 thermal luminosity. It is consistent with the NS cooling theory and provides certain constraints on the NS model parameters. We found that J1957 is one of the coldest middle-aged NSs with measured effective temperatures: its redshifted thermal luminosity is $L^\infty \approx (0.2 - 1.0) \times 10^{30}$ erg s^{-1}. This indicates that J1957 has already passed from a relatively slow neutrino cooling stage to a significantly faster photon stage. The X-ray pulse-profile with a single pulse per period and with the pulse fraction of 18 ± 6 per cent constraints the pulsar viewing geometry $30^\circ \lesssim \alpha + \zeta \lesssim 90^\circ$.

Using the interstellar extinction–distance relation, we estimated the distance to the pulsar to be of $\approx$0.1–1 kpc. Spectral fits with atmosphere models imply a most probable distance of 200–300 pc.

We also detected a weak $\sim$8 arcmin long trail-like feature connected with the pulsar. It most likely can be a PWN or a misaligned outflow powered by the pulsar.

Deeper X-ray observations are needed for more stringent constraints on the properties of the pulsar and the trail-like nebula. Phase-resolved analysis of such data could be helpful to understand the pulsar geometry. Measurement of the pulsar's p.m. in X-rays is necessary to understand the nature of the nebula. Due to the low extinction and the likely proximity of J1957, it seems to be a good candidate for UV/optical observations. This could confirm the low temperature and lead to more accurate distance estimate.

ACKNOWLEDGEMENTS

We would like to thank the anonymous referee for useful comments and A. A. Danilenko for helpful discussion. The work was partially supported by the Russian Foundation for Basic Research (RFBR) according to the project 19-52-12013. VFS thanks Deutsche Forschungsgemeinschaft (DFG) for financial support (grant WE 1312/53-1). His work was also partially funded by the subsidy 0671-2020-0052 allocated to Kazan Federal University for the state assignment in the sphere of scientific activities. DAZ thanks Pirinem

School of Theoretical Physics for hospitality. The scientific results reported in this article are based on observations obtained with *XMM–Newton*, an ESA science mission with instruments and contributions directly funded by ESA Member States and NASA.

DATA AVAILABILITY

The X-ray data are available through their respective data archives: https://www.cosmos.esa.int/web/xmm-newton/xsa for *XMM–Newton* data and https://cxc.harvard.edu/cda/ for *Chandra* data.

REFERENCES

Abdo A. A. et al., 2013, ApJS, 208, 17
Arnaud K., Gordon C., Dorman B., 2018, Xspec: an X-Ray spectral fitting package. Users' Guide for version 12.10.1. Available at: https://heasarc.gsfc.nasa.gov/xanadu/xspec/manual/XspecManual.html
Auchettl K. et al., 2015, ApJ, 802, 68
Baldo M., Schulze H. J., 2007, Phys. Rev. C, 75, 025802
Beloborodov A. M., 2002, ApJ, 566, L85
Blouin S., Shaffer N. R., Saumon D., Starrett C. E., 2020, ApJ, 899, 46
Brazier K. T. S., 1994, MNRAS, 268, 709
Brownsberger S., Romani R. W., 2014, ApJ, 784, 154
Buccheri R. et al., 1983, A&A, 128, 245
Capitanio L., Lallement R., Vergely J. L., Elyajouri M., Monreal-Ibero A., 2017, A&A, 606, A65
Cash W., 1979, ApJ, 228, 939
Chang C., Pavlov G. G., Kargaltsev O., Shibanov Y. A., 2012, ApJ, 744, 81
Cutri R. M., et al., 2014, VizieR Online Data Catalog, II/328
Ding D., Rios A., Dussan H., Dickhoff W. H., Witte S. J., Carbone A., Polls A., 2016, Phys. Rev. C, 94, 025802
Elgarøy Ø., Engvik L., Hjorth-Jensen M., Osnes E., 1996, Phys. Rev. Lett., 77, 1428
Flewelling H. A. et al., 2020, ApJS, 251, 7
Foight D. R., Güver T., Özel F., Slane P. O., 2016, ApJ, 826, 66
Foreman-Mackey D., Hogg D. W., Lang D., Goodman J., 2013, PASP, 125, 306
Ginzburg V. L., Ozernoy L. M., 1965, Sov. Phys. JETP, 20, 689
Goodman J., Weare J., 2010, Commun. Appl. Math. Comput. Sci., 5, 65
Greenstein G., Hartke G. J., 1983, ApJ, 271, 283
Ho W. C. G., Potekhin A. Y., Chabrier G., 2008, ApJS, 178, 102
Ho W. C. G., Elshamouty K. G., Heinke C. O., Potekhin A. Y., 2015, Phys. Rev. C, 91, 015806
Hobbs G., Lorimer D. R., Lyne A. G., Kramer M., 2005, MNRAS, 360, 974
Kargaltsev O., Pavlov G. G., 2008, in Bassa C., Wang Z., Cumming A., Kaspi V. M., eds, AIP Conf. Proc. Vol. 983, 40 Years of Pulsars: Millisecond Pulsars, Magnetars and More. Am. Inst. Phys., New York, p. 171
Kargaltsev O., Pavlov G. G., Klingler N., Rangelov B., 2017, J. Plasma Phys., 83, 635830501
Kerr M., Ray P. S., Johnston S., Shannon R. M., Camilo F., 2015, ApJ, 814, 128
Lallement R., Vergely J. L., Valette B., Puspitarini L., Eyer L., Casagrande L., 2014, A&A, 561, A91
Lallement R. et al., 2018, A&A, 616, A132
Manchester R. N., Taylor J. H. J., 1977, Pulsars. W. H. Freeman & Co., San Francisco
Marelli M. et al., 2013, ApJ, 765, 36
Marelli M., Mignani R. P., De Luca A., Saz Parkinson P. M., Salvetti D., Den Hartog P. R., Wolff M. T., 2015, ApJ, 802, 78
Margueron J., Sagawa H., Hagino K., 2008, Phys. Rev. C, 77, 054309
Mignani R. P., Pavlov G. G., Kargaltsev O., 2010, ApJ, 720, 1635
Misner C. W., Thorne K. S., Wheeler J. A., 1973, Gravitation. W. H. Freeman and Co., San Francisco
Müller B., 2020, Living Rev. Comput. Astrophys., 6, 3
Pavlov G. G., Zavlin V. E., 2000a, in Martens P. C. H., Tsuruta S., Weber M. A., eds, Proc. IAU Symp. 195, Highly Energetic Physical Processes and Mechanisms for Emission from Astrophysical Plasmas. Astron. Soc. Pac., San Francisco, p. 103
Pavlov G. G., Zavlin V. E., 2000b, ApJ, 529, 1011
Pearson J. M., Chamel N., Potekhin A. Y., Fantina A. F., Ducoin C., Dutta A. K., Goriely S., 2018, MNRAS, 481, 2994
Pechenick K. R., Ftaclas C., Cohen J. M., 1983, ApJ, 274, 846
Pierbattista M., Harding A. K., Grenier I. A., Johnson T. J., Caraveo P. A., Kerr M., Gonthier P. L., 2015, A&A, 575, A3
Potekhin A. Y., Chabrier G., 2003, ApJ, 585, 955
Potekhin A. Y., Chabrier G., 2018, Astron. Astrophys., 609, A74
Potekhin A. Y., Yakovlev D. G., Chabrier G., Gnedin O. Y., 2003, ApJ, 594, 404
Potekhin A. Y., Lai D., Chabrier G., Ho W. C. G., 2004, ApJ, 612, 1034
Potekhin A. Y., Chabrier G., Ho W. C. G., 2014, A&A, 572, A69
Potekhin A. Y., Zyuzin D. A., Yakovlev D. G., Beznogov M. V., Shibanov Y. A., 2020, MNRAS, 496, 5052
Poutanen J., Beloborodov A. M., 2006, MNRAS, 373, 836
Reynolds S. P., Pavlov G. G., Kargaltsev O., Klingler N., Renaud M., Mereghetti S., 2017, Space Sci. Rev., 207, 175
Saz Parkinson P. M. et al., 2010, ApJ, 725, 571
Schlafly E. F., Meisner A. M., Green G. M., 2019, ApJS, 240, 30
Spitkovsky A., 2006, ApJ, 648, L51
Sturrock P. A., 1971, ApJ, 164, 529
Suleimanov V., Potekhin A. Y., Werner K., 2009, A&A, 500, 891
Takatsuka T., Tamagaki R., 2004, Prog. Theor. Phys., 112, 37
Taverna R., Turolla R., Suleimanov V., Potekhin A. Y., Zane S., 2020, MNRAS, 492, 5057
Thorne K. S., 1977, ApJ, 212, 825
Willatt R., Ehle M., 2016, Guide for use of the images script. Available at: https://www.cosmos.esa.int/documents/332006/641121/README.pdf
Wilms J., Allen A., McCray R., 2000, ApJ, 542, 914
Yakovlev D. G., Pethick C. J., 2004, ARA&A, 42, 169
Yakovlev D. G., Gnedin O. Y., Gusakov M. E., Kaminker A. D., Levenfish K. P., Potekhin A. Y., 2005, Nucl. Phys. A, 752, 590
Zavlin V. E., 2009, in Becker W., ed., Astrophysics and Space Sci. Library, Vol. 357, Neutron Stars and Pulsars. Springer, Berlin, p. 181
Zharikov S., Mignani R. P., 2013, MNRAS, 435, 2227
Zharikov S., Shibanov Y., Komarova V., 2006, Adv. Space Res., 37, 1979

APPENDIX A: ATMOSPHERE MODELS FOR NEUTRON STARS WITH DIPOLE MAGNETIC FIELDS

Magnetized plane-parallel NS atmosphere models are computed using an advanced version of the code described in Suleimanov, Potekhin & Werner (2009). The code has been modified to account for different inclinations θ_B of the magnetic field with respect to the local surface normal. Hydrogen composition is considered, taking into account incomplete ionization at relatively low temperatures. The effects of the strong magnetic field and the atomic thermal motion across the field on the plasma opacities are treated following Potekhin & Chabrier (2003) with the improvements described in Potekhin, Chabrier & Ho (2014). Polarization vectors and opacities of normal electromagnetic modes are calculated as in Potekhin et al. (2004).

Physical models of emission from NSs should take into account magnetic field and temperature distributions over the surface. We assume a dipolar magnetic field, after accounting for the effect of General Relativity, according to Ginzburg & Ozernoy (1965) (see also Pavlov & Zavlin 2000b):

$$B = B_{\rm p}\sqrt{\cos^2\gamma + f^2\sin^2\gamma/4}, \quad \cos\theta_B = (B_{\rm p}/B)\cos\gamma, \qquad \text{(A1)}$$

where B is the field strength, θ_B is the field inclination to the surface normal at a magnetic colatitude γ,

$$f = \frac{2}{\sqrt{1-u}} \frac{u^2 - 2u - 2(1-u)\ln(1-u)}{u^2 + 2u + 2\ln(1-u)}, \tag{A2}$$

$u = r_g/R$ is the compactness parameter, $r_g = 2GM/c^2$ is the gravitational radius, G is the gravitational constant, and c is the speed of light. The distribution of local effective temperature T_s over the stellar surface is calculated using the results of Potekhin et al. (2003). In order to minimize model dependence, we assume the T_s-distribution of an iron heat-blanketing envelope. This assumption does not change our results since, for any chemical composition of the envelope, the dependence of T_s on θ_B is similar to that given in Greenstein & Hartke (1983).

Model atmospheres for an inclined magnetic field require solving the transfer problem in two dimensions. The optical properties of the magnetized plasma depend on the angle η between the photon wave vector $\boldsymbol{k}$ and the local magnetic field $\boldsymbol{B}$. On the other hand, under the plane-parallel approximation the radiation field naturally depends on the angles (θ_k, ϕ_k), where θ_k is the angle between $\boldsymbol{k}$ and the surface normal and ϕ_k is the angle between the projections of $\boldsymbol{k}$ and $\boldsymbol{B}$ on the surface. To avoid interpolation of the opacities over such a 2D grid, the code solves the transfer problem over an (η, ψ) angular grid, where ψ is the azimuth associated to the polar angle η, and then the transformation between the angular coordinates (η, ψ) and (θ_k, ϕ_k) is used (see Taverna et al. 2020 for more details):

$$\cos\eta = \sin\theta_B \sin\theta_k \cos\phi_k + \cos\theta_B \cos\phi_k, \tag{A3}$$

$$\cos\psi = \frac{\cos\theta_k - \cos\eta\cos\theta_B}{|\sin\eta\sin\theta_B|}. \tag{A4}$$

The photon wavevector at infinity $\boldsymbol{k}'$ differs from $\boldsymbol{k}$ at the surface due to gravitational redshift and light-bending (Pechenick, Ftaclas & Cohen 1983; Pavlov & Zavlin 2000b). The photon energy at infinity is smaller than the photon energy at the surface by factor $\sqrt{1-u} = 1/(1+z_g)$, where z_g is gravitational redshift. The period of PSR J1957+5033 is sufficiently long so that we can assume that the stellar surface is spherical and neglect the effects of rotation (see e.g. Poutanen & Beloborodov 2006 for description of these effects). Let us consider a surface element $\mathrm{d}S = R^2\,\mathrm{d}\cos\vartheta\,\mathrm{d}\varphi$, where ϑ and φ are the polar and azimuthal angles. For the relation between ϑ and θ_k we use approximation (Beloborodov 2002)

$$1 - \cos\vartheta = (1-\cos\theta_k)/(1-u). \tag{A5}$$

The flux observed from this surface element is proportional to the specific intensity I_E^∞ and the solid angle $\mathrm{d}\Omega$ occupied by this element on the observer's sky. This solid angle equals (Beloborodov 2002)

$$\mathrm{d}\Omega = \frac{\mathrm{d}S\cos\theta_k}{D^2} \frac{1}{1-u} \frac{\mathrm{d}\cos\theta_k}{\mathrm{d}\cos\theta_k'}, \tag{A6}$$

where θ_k' is the angle between the local normal to the surface and the photon momentum at infinity. Without loss of generality we can choose the polar coordinate axis along the line of sight; then $\theta_k' = \vartheta$. Since I_E/E^3 is invariant (Misner, Thorne & Wheeler 1973, Section 22.6), the observed specific intensity I_E^∞ is related to the emitted intensity I_E by a constant redshift factor $I_E^\infty = I_E/(1+z_g)^3$. Thus the flux is

$$\mathrm{d}F_E^\infty = I_E^\infty \mathrm{d}\Omega = \frac{R^2\cos\theta_k}{D^2} \frac{I_E}{(1+z_g)^3}\,\mathrm{d}\varphi\,\mathrm{d}\cos\vartheta. \tag{A7}$$

The monochromatic spectral flux density is then computed by integrating the emission from different local patches over the stellar surface. Making use of equation (A6), we obtain[7]

$$F_E^\infty = \frac{R^2}{D^2(1+z_g)} \int_0^{2\pi}\mathrm{d}\varphi \int_0^{\pi/2} I_E(\theta_k,\phi_k)\cos\theta_k \sin\theta_k \mathrm{d}\theta_k. \tag{A8}$$

For an axisymmetric magnetic field, the angle ϕ_k and the magnetic colatitude γ are determined at every θ_k and φ by the relations (cf. Ho et al. 2008)

$$\cos\gamma = \cos\varphi\sin\vartheta\sin\Theta_m + \cos\vartheta\cos\Theta_m, \tag{A9}$$

$$\cos\phi_k = \frac{\cos\gamma\cos\vartheta - \cos\Theta_m}{|\sin\gamma\sin\vartheta|}, \tag{A10}$$

where Θ_m is the angle between the magnetic axis and line of sight. The integration in equation (A8) is restricted by those angles θ_k that correspond to real values of ϑ.

For each neutron star parameter set, the local plane-parallel atmosphere models are computed at the magnetic pole and at three magnetic latitudes between the pole and the equator, according to Table A1. The atmosphere model at the equator needs not to be calculated, because temperature at low latitudes is so low that it cannot noticeably affect the observed flux (in practice, we use the blackbody spectrum at the equator, but we have checked that with alternative models F_E^∞ remains the same within 3 per cents). At each fixed magnetic colatitude γ, the opacities, polarizabilities, and EoS of the hydrogen plasma were computed on a fixed grid of plasma temperature and density, from which the values required during the radiative-transfer calculation were obtained by interpolation.

To calculate the integral (A8), the specific intensity I_E is evaluated at arbitrary γ, E, θ_k, and ϕ_k from the computed values by interpolation. It should be noted that B-dependent absorption features would produce series of lines, if we kept E fixed during this interpolation. In reality, such features are broadened due to the smooth variation of B with γ. In order to reproduce this broadening and thus get rid of the non-physical series of lines, we first remap our calculated I_E as a function of ratio E/B and then interpolate it in θ_k, ϕ_k, and $B(\gamma)$ for every fixed E/B (cf. Ho et al. 2008). The result of such integration is shown in Fig. A1.

The local effective temperature T_s and the global effective temperature $T_{\rm eff}$ are defined by the Stefan–Boltzmann law

$$\sigma_{\rm SB}T_s^4 = F_r, \quad 4\pi R^2\sigma_{\rm SB}T_{\rm eff}^4 = L_r \tag{A11}$$

where

$$F_r = \int_0^\infty \mathrm{d}E \int_0^{2\pi}\mathrm{d}\phi_k \int_0^{\pi/2} I_E(\theta_k,\phi_k)\cos\theta_k\sin\theta_k\,\mathrm{d}\theta_k \tag{A12}$$

is the local flux density, which depends on the magnetic colatitude γ, and

$$L_r = R^2\int_0^{2\pi}\mathrm{d}\varphi\int_0^{\pi} F_r(\gamma)\,\sin\vartheta\,\mathrm{d}\vartheta \tag{A13}$$

is the local bolometric luminosity. The redshifted ('apparent') luminosity, effective temperature and radius as detected by a distant observer are (e.g. Thorne 1977)

$$L^\infty = L_r/(1+z_g)^2 = 4\pi\sigma_{\rm SB}(T^\infty)^4(R^\infty)^2, \tag{A14}$$

$$T^\infty = T_{\rm eff}/(1+z_g), \quad R^\infty = R(1+z_g). \tag{A15}$$

[7] This is equivalent to equation (8) of Ho et al. (2008), where we have restored the missed factor $\cos\theta_k$.

Table A1. Parameter sets used in calculation of atmosphere models: cosines of magnetic colatitude γ and magnetic field inclination θ_B, logarithms of magnetic field strength B, and local effective temperatures T_s.

lg T^∞ (K)			5.1	5.2	5.3	5.4	5.5	5.6	5.7
cos γ	cos θ_B	lg B (G)				lg T_s (K)			
NSMDIP 1: $M = 1.4$ M$_\odot$, $R = 12.6$ km ($z_g = 0.22$), $B_p = 3 \times 10^{12}$ G									
0.25	0.424	12.25	5.075	5.183	5.285	5.383	5.483	5.583	5.684
0.50	0.724	12.32	5.188	5.292	5.393	5.492	5.591	5.691	5.791
0.75	0.900	12.40	5.238	5.337	5.437	5.537	5.637	5.737	5.837
1	1	12.48	5.266	5.361	5.459	5.560	5.661	5.762	5.861
NSMDIP 2: $M = 2$ M$_\odot$, $R = 11.4$ km ($z_g = 0.44$), $B_p = 3 \times 10^{12}$ G									
0.25	0.398	12.28	5.139	5.246	5.348	5.447	5.546	5.647	5.748
0.44	0.633	12.32	5.236	5.340	5.442	5.541	5.640	5.740	5.840
0.73	0.875	12.40	5.308	5.408	5.508	5.608	5.708	5.807	5.907
1	1	12.48	5.341	5.437	5.535	5.636	5.737	5.837	5.937
NSMDIP 3: $M = 1.4$ M$_\odot$, $R = 12.6$ km ($z_g = 0.22$), $B_p = 1.1 \times 10^{12}$ G									
0.19	0.335	11.80	5.037	5.137	5.236	5.337	5.439	5.542	5.645
0.56	0.775	11.90	5.206	5.306	5.405	5.505	5.605	5.705	5.805
0.87	0.953	12.00	5.249	5.349	5.450	5.550	5.650	5.749	5.848
1	1	12.04	5.260	5.359	5.461	5.561	5.661	5.760	5.859

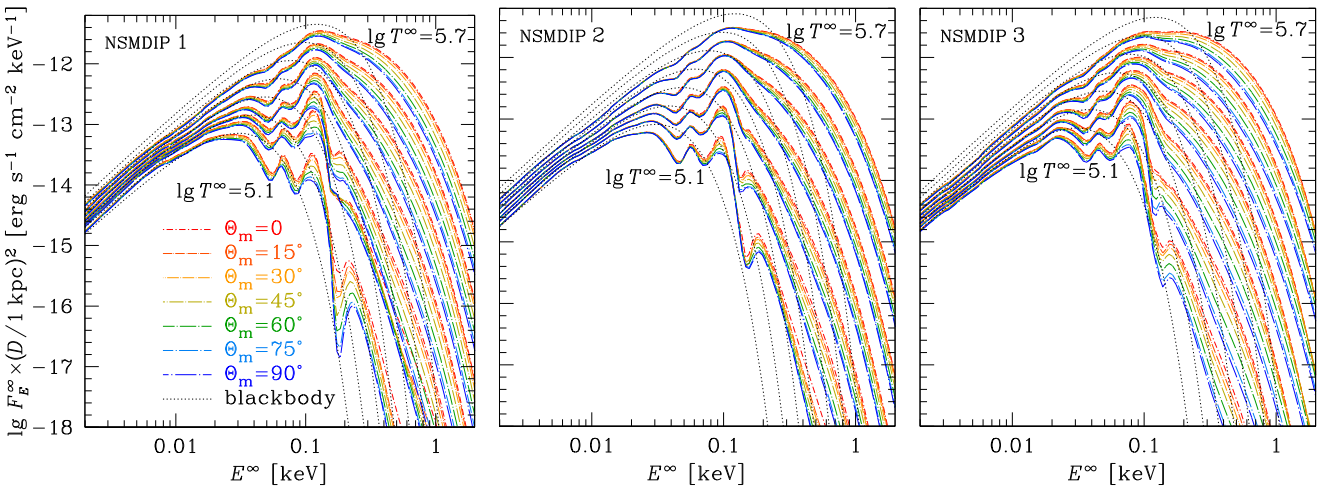

Figure A1. Unabsorbed redshifted spectral flux density as function of redshifted energy, calculated according to equation (A8) for models 1, 2, and 3 listed in Table A1 (left-hand, middle, and right-hand panels, respectively) for different inclinations Θ_m of magnetic dipole axis (drawn with different line styles, according to the legend) and redshifted effective temperatures (lg T^∞ (K) = 5.1, 5.2, 5.3, 5.4, 5.5, 5.6, and 5.7, from bottom to top). For comparison, the BB spectra at the same temperatures are shown by dotted lines.

For each model (NSMDIP 1, 2 or 3), we fix radius R, redshift z_g and B_p to the values indicated in Table A1 and treat the effective temperature T^∞, magnetic axis inclination Θ_m and distance D as continuous adjustable parameters to fit the observed spectral fluxes using calculated grids of F_E^∞ .

In the axisymmetric model, the pulsar geometry is determined by the angles α and ζ that the spin axis makes with the magnetic axis and with the line of sight, respectively (e.g. Pavlov & Zavlin 2000b). To produce phase-resolved spectra, it is sufficient to calculate

$$\cos\Theta_m = \sin\zeta\,\sin\alpha\,\cos\phi + \cos\alpha\,\cos\zeta \qquad \text{(A16)}$$

for each rotation phase ϕ. Some light curves computed by integration of such phase-resolved spectra are shown in Fig. 9.

APPENDIX B: INTERSTELLAR ABSORPTION–DISTANCE RELATION

We estimated the distance to J1957 including the interstellar absorption–distance relation shown in Fig. B1 as a prior in the fitting procedure. The relation was derived in the following way. We used the 3D map of the local interstellar medium presented in https://stilism.obspm.fr/ (see Lallement et al. 2014; Capitanio et al. 2017; Lallement et al. 2018 for details) to obtain the relation between the interstellar extinction $E(B-V)$ and the distance D in the pulsar direction. Then $E(B-V)$ was converted to the X-ray absorbing column density N_H utilizing the relation by Foight et al. (2016). We used linear interpolation to derive the N_H–D dependence between the obtained points.

We also independently estimated the maximum absorption in the pulsar direction using two brightest extragalactic X-ray sources in the J1957 field with coordinates R.A., Dec. = ($19^h57^m16\overset{s}{.}491$, $+50^\circ40'17\overset{''}{.}280$) and R.A., Dec. = ($19^h56^m48\overset{s}{.}205$, $+50^\circ39'32\overset{''}{.}101$). They have optical counterparts in the Pan-STARRS (Flewelling et al. 2016) and *WISE* (Cutri & et al. 2014; Schlafly, Meisner & Green 2019) catalogues and are detected with the optical monitor (OM) on-board *XMM–Newton*. According to their spectral energy distributions, the sources are active galactic nuclei (AGNs). We extracted their X-ray spectra, grouped them to ensure at least 25

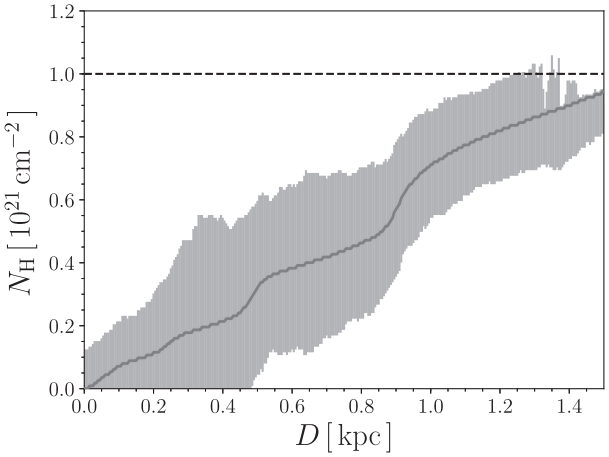

Figure B1. The relation between the interstellar absorption $N_{\rm H}$ and the distance D (the dark grey line) with uncertainties shown in light grey in the direction towards J1957. The dashed black line shows the maximum $N_{\rm H}$ derived from the spectral analysis of two AGNs in the pulsar field (see the text for details).

counts per energy bin and fitted with the absorbed model for AGN OPTXAGN. The resulting column density $N_{\rm H}$ shown by the dashed black line in Fig. B1 is about 10^{21} cm^{-2} which is in agreement with the value obtained from the $E(B-V)$–D relation.

The spectral models which we used to describe the pulsar thermal emission includes the ratio of the emitting area radius and the distance as a parameter. Implementation of the $N_{\rm H}$–D relation allowed us to separate it into two independent parameters.

This paper has been typeset from a TEX/LATEX file prepared by the author.